ACS APPLIED MATERIALS & INTERFACES

www.acsami.org Research Article

Multifunctional Sensors Based on Doped Indium Oxide Nanocrystals

Chang Shu,[‖] Nan Zhang,[‖] Yiyuan Gao,[‖] Junru An, Xin Wen, Wanli Ma, Zeke Liu,* Baoquan Sun,* and Shaojuan Li*

Cite This: *ACS Appl. Mater. Interfaces* 2022, 14, 24648−24658 Read Online

ACCESS | Metrics & More | Article Recommendations | SI Supporting Information

ABSTRACT: There is an increasing need for multifunctional sensors that can detect radiation, biological activity, gas, etc. for efficient health monitoring, neurological medical devices, and human−machine interfaces in recent years. Herein, we demonstrated a multifunctional Sn-doped In_2O_3 nanocrystal (ITO NC) based device for ulyoutraviolet (UV)/infrared (IR) dual-band photodetection and light-activated efficient nitrogen dioxide (NO_2) gas sensing at room temperature (RT). The effects of different surface ligands and annealing process of ITO NCs on their photodetection performance were investigated. The ITO NCs capped with 1,2-ethanedithiol (EDT) show a responsivity of 31.3/177.7 mA W^{-1} and normalized detectivity of $\sim 1 \times 10^{10}/10^9$ cm $Hz^{1/2}$ W^{-1} under UV/IR illumination at 375/2200 nm at RT. The potential of the ITO NCs sensors to monitor low concentrations of NO_2 is activated by light illumination. The sensor has a higher response (4.2) to 1 ppm of NO_2, shorter response/recovery time (156.8/554.2 s), and a lower detection limit (LOD) (219 ppb) under UV illumination compared within a dark environment. The LOD of the sensor is lower than the allowable exposure limit of NO_2 specified in “Air Pollutant Limits” of the Occupational Safety and Health Administration (OSHA). Our work paves an alternative platform for the development of low-cost, integration-friendly multifunctional devices.

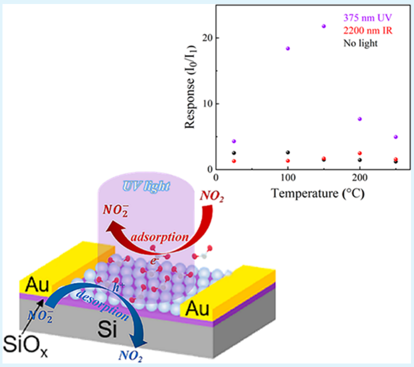

KEYWORDS: *ITO nanocrystal, multifunctional sensors, dual-band photodetection, gas sensor, room temperature*

■ INTRODUCTION

With the rapid development of portable devices and Internet of Things, the need for integration of sensors has accelerated the research of multifunctional sensing platforms. Multifunctional sensors that can detect light radiation, biological activities, stress, and gases in order to monitor environmental changes have great potential applications, enabling efficient health monitoring, neurological medical devices, human−machine interfaces, and other integrated smart microsystems.[1,2] Currently, the well-known multifunctional sensors combining pressure/stress sensor with humidity sensor for human−machine interaction have provided abundant information from the human body surroundings, being beneficial for evaluation of health states. A multifunctional sensor that is sensitive to touch or temperature can find important application in prosthetics for the disabled.[3] On the other hand, various types of gas sensors have been developed to monitor the harmful gas content in the atmosphere.[4] For instance, hybridization of ultraviolet (UV) photosensitive semiconductor with gas sensing capability is a feasible approach to generate such multifunctional devices. Tracking environmental conditions, including concentration of harmful gas, ambient temperature, UV radiation, etc., provides valuable information for human activity monitoring and personal telemedicine care.

The development and synthesis of multifunctional materials are a prerequisite for constructing multifunctional devices and understanding the design rules of next-generation hybrid functional systems. One specific concern with these materials is that they should meet the requirements of miniaturization and planar integration. In addition to multiple functions, the sensor should also have high sensitivity, low power consumption, and low cost. Silicon materials, currently prevalent in the semiconductor field, have been successfully utilized for photodetection, biological sensing, gas sensing, etc.[5] However, the inherent difficulties of their integration onto arbitrary substrates have limited their applicability. As an alternative, in recent years, plasmonics has become a hot area for studying light−matter interactions,[6,7] and surface plasmon resonances (SPs) in nanomaterials has been successfully used in light detection, gas sensing, biological sensing, etc.,[8−10] owing to their outstanding physical and chemical properties, such as abundant chemical active sites, high surface-to-volume ratio, and tunable light absorption. Materials with SPs effect have renewed opportunities in designing and assembling different sensing mechanisms in realizing multifunctional sensors. SPs exist at the interface between noble metal and dielectric or

Received: March 25, 2022
Accepted: May 6, 2022
Published: May 17, 2022

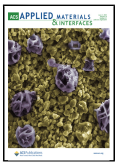

https://doi.org/10.1021/acsami.2c05280

localized on the surface of metal alloys and heavily doped semiconductors nanoparticles.[11] Conventional SPs mediums are mainly made of noble metal materials, and their SP absorption is mainly concentrated in the visible range due to the high carrier concentration of noble metal materials. In contrast, doped semiconductor NCs can easily achieve SP absorption in the near- to mid-IR range by modulating the doping concentration.[12] These include defect-doped sulfur and phosphorus copper compounds ($Cu_{2-x}S$, $Cu_{2-x}Se$, $Cu_{2-x}Te$, $Cu_{3-x}P$),[13] doped metal oxides,[14−16] and silicon NCs.[17] Compared with the strong visible resonance absorption in noble metal nanoparticles,[18] doped metal oxides are gradually becoming a hot spot for IR optoelectronic research due to their low cost and easy tunability of IR absorption by changing its doping concentration.[19] Doped metal oxide NCs have high light absorption efficiencies in the near/mid-IR region. For example, typical Sn-doped In_2O_3 NCs (ITO NCs) can reach a molar extinction coefficient of 10^8 M^{-1} cm^{-1}, which is 2 orders of magnitude higher than that of PbS and PbSe quantum dots in the same wavelength band.[20] On the other hand, ITO has been widely used as transparent electrode material in light-emitting diodes,[21−23] solar cells,[24] and touch screens.[25] In this regard, ITO NCs not only have good visible light transmittance but also can realize the controlled adjustment of its IR plasmon resonance absorption.[19] In addition, due to the intrinsic bandgap absorption (3.55−3.75 eV), ITO NCs also exhibit excellent absorption properties in the UV band, which provides a material basis for the preparation of dual-band photodetection in UV and IR regimes. Moreover, it is worth noting that In_2O_3, due to its wide bandgap and low resistivity, is a promising gas-sensitive material as well.[26] In recent years, In_2O_3 nanomaterials with different morphologies have been synthesized and utilized for gas sensing, such as nanoparticles, nanoflowers, nanosheets, nanowires, and so on.[27,28] According to reports, heteroatom doped In_2O_3 can change the properties of the material, such as carrier concentration, defect state, particle size, etc., which can effectively improve the gas sensitivity of the material. For example, Ce-doped In_2O_3 nanostructures show good sensitivity to ethylene glycol at 240 °C.[29] The sensing performance of Pr-doped In_2O_3 nanoparticles to ethanol is better than that of pure In_2O_3.[26] However, these gas sensors typically operate at high temperatures of 200−500 °C, as they require thermal energy to activate the adsorbed gas and to overcome energy barriers to satisfy sensing response. High operating temperatures may increase the complexity of fabrication and cause attenuation of sensor sensitivity due to thermally induced maturation of nanoparticles. Therefore, many research results have been devoted to the development of gas sensors that can operate at lower temperatures or even at RT.[30] In this regard, photoactivation is a promising alternative to heat source. It has been reported that irradiating semiconductor materials with light can change the surface electronic properties by adjusting the concentration of photogenerated carriers, thereby improving the sensor sensitivity and response/recovery speed at RT.[31] Thereby, exploring novel materials with both photosensitivity and gas sensitivity is nontrivial to the development of multifunctional sensing system.

While important progress has been made on research of ITO based optoelectronic devices, the developed devices at present usually only have a single function for the target, which cannot meet the requirement of multifunctional sensing platform. From the above description, we expected that ITO NCs are promising materials for low-cost, high performance multifunctional sensing devices, due to their impressive resonance light absorption, abundant chemical active sites, high surface-to-volume ratio, and ease of processing, but the function hybridizations are rarely explored so far. In this paper, we construct a multifunctional sensing device based on ITO NCs. The multifunctional devices achieve visible-blind dual-band photodetection in UV and IR regimes and light-activated NO_2 gas detection at RT. The device prepared by using 10% Sn-doped ITO NCs can obtain a significant photoresponse in the 2200 nm with a maximum responsivity of 177.7 mA W^{-1} and a normalized detectivity of ~1 × 10^9 cm $Hz^{1/2}$ W^{-1}. Its response band is close to the mid-IR and can achieve both UV light detection with a normalized detectivity of ~1.3 × 10^{10} cm $Hz^{1/2}$ W^{-1} at 375 nm at RT. Notably, barely no response in the visible range was observed for pure ITO NCs. Under UV irradiation, ITO NCs exhibited significantly higher response to NO_2 (4.2−1 ppm of NO_2), shorter response/recovery speeds (156.8/554.2 s), and low LOD (219 ppb) compared with in the dark. Our multifunctional sensing system provides a new platform for emerging miniaturized and integrated sensors that hold potential applications in fire rescue, monitoring of lung inflammation, and prevention of skin damage caused by UV light.

■ EXPERIMENTAL SECTION

Preparation of ITO NCs. ITO NCs with tunable Sn doping concentration were prepared based on the previously reported method.[32] In a typical synthesis of 10% ITO NCs, 1.8 mmol of indium(III) acetate and 0.2 mmol of tin(IV) acetate were mixed with 4 mL of oleic acid in a 25 mL flask. After degassing under vacuum for 1 h at 100 °C, the mixture was heated at 150 °C for 30 min to promote the formation of metal oleate precursors. In another reaction flask, 26 mL of oleyl alcohol was vacuum-dried at 100 °C for 1 h before being heated to 275 °C under N_2 atmosphere. Afterward, the metal precursor solution was added dropwise via a syringe pump (~0.13 mL/min) into the flask containing oleyl alcohol. After completion of injection, the reaction mixture was kept at 275 °C for another 10 min before being cooled to RT. The NCs were isolated by precipitation with isopropanol and centrifugation at 6000 rpm for 5 min. The NCs were redispersed in ~20 mL of hexane and centrifuged at 3000 rpm for 3 min to remove large aggregates. Following another round of isopropanol precipitation and centrifugation, the ITO NCs were finally dispersed in octane (5 mg mL^{-1}) for device fabrication.

Ligand Exchange of ITO NCs. EDT (0.1% v/v in acetonitrile), MPA (1% v/v in methanol), and MAI (10 mg mL^{-1} in methanol) are used to exchange the native oleate ligand on ITO NCs. The ITO NC solution (5 mg mL^{-1} in octane) was spin-coated onto quartz or silicon substrate. Then, ~0.2 mL of exchange solution was dropped onto the NC film for 30 s, followed by two rinse−spin steps with the pure solutions (acetonitrile or methanol). The above ligand exchange process was repeated for one more round.

Device Preparation and Characterization. ITO NC photodetectors were fabricated on SiO_2/Si substrates. After spin-coating ITO NCs, ligand exchange was first performed. Then, Au or Ag metal electrodes were evaporated by thermal evaporation. The morphologies of the ITO NCs were characterized using transmission electron microscopy (TEM, FEI Tecnai F30). The absorption spectra of the films were measured by UV−vis−NIR spectrophotometer. The valence band and Fermi energy level positions of the NCs were analyzed by ultraviolet photoelectron spectroscopy (UPS). Electrical characterization was carried out at RT and under vacuum conditions by an equipped probe stage as well as a semiconductor property analyzer (Keithley 4200).

Sensor Measurements. The gas sensor measurement is carried out in an enclosed temperature-controlled probe station (Instec, hcp421v-pm) equipped with a Keithley 4200 semiconductor

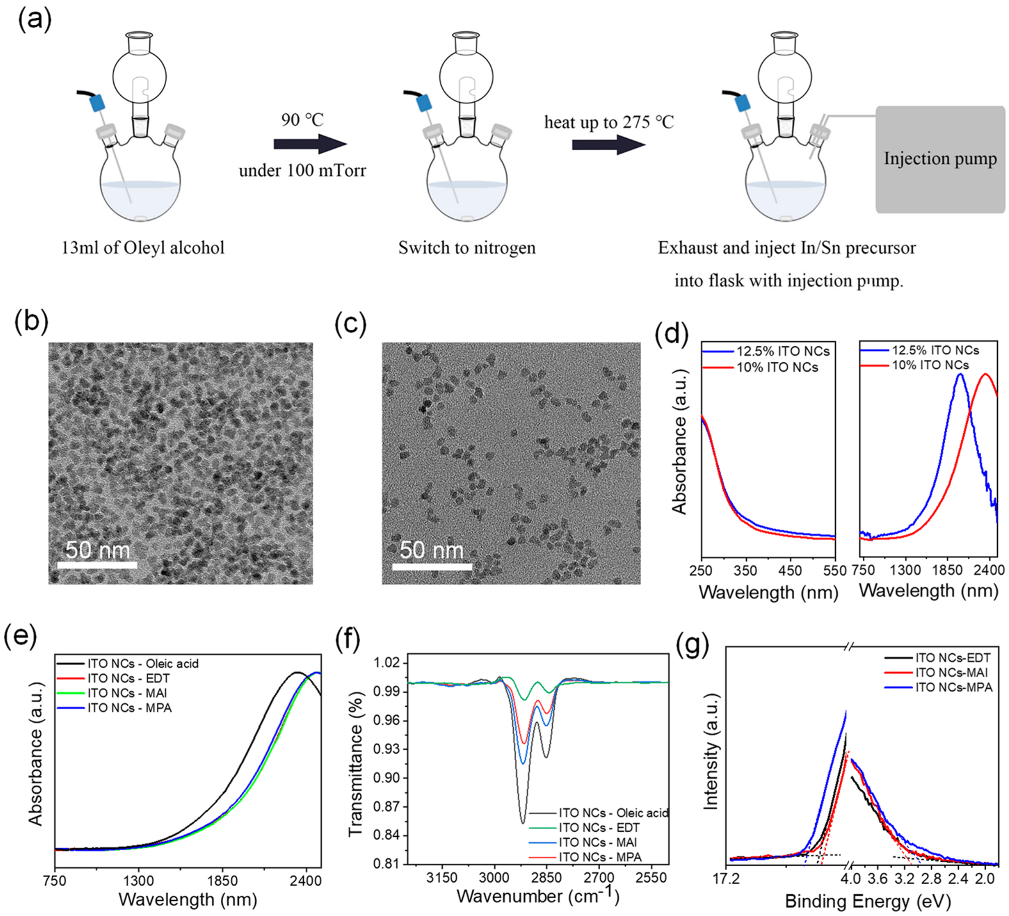

Figure 1. ITO NCs with different doping concentrations. (a) Experimental flowchart for the synthesis of ITO NCs. TEM images of (b) 10% and (c) 12.5% Sn-doped ITO NCs. (d) UV−vis−NIR absorption spectra of ITO NCs at different doping concentrations without ligand exchange. (e) UV−vis−NIR absorption spectra and (f) FTIR measurement results of ITO NCs with 10% Sn doping after different ligand exchanges. (g) UPS results of ITO NCs with 10% Sn doping after different ligand exchanges.

characterization system to monitor current changes. Three mass flow controllers (MFC, Sevenstar, CS-200A) realize the change of NO_2 concentration from 0.2 to 100 ppm by changing the flow ratio between NO_2 and N_2. The desired concentration and flux of NO_2 gas were obtained from mass flow controllers by mixing N_2 diluted 100 ppm of NO_2 gas and 99.999% N_2 gas. The gas pressure during measurement of gas sensing is at 101.325 kPa. Two irradiating lasers with wavelengths of 375 and 2200 nm are used during the experiments. The distance between the light source and the sensor and light intensity is fixed at 20 cm and 12.5 mW·cm^{-2}. The gas sensing experiments are carried out under different temperatures (25 °C, 100 °C, 150 °C, 200 °C, and 250 °C) and different wavelengths of light. The applied bias voltage of the device is set to 1 V.

■ RESULTS AND DISCUSSION

Characterization of ITO NCs. ITO NCs were prepared according to the previous work.[32] The experimental flowchart of synthesis of ITO NCs is shown in Figure 1a, where the precursor solution of the metal oleate complex is slowly injected into the oleyl alcohol solution at a certain rate, resulting in the generation of ITO NCs due to the rapid esterification reaction. The details of synthesis process are described in the Experimental Section. By varying the ratio of indium and tin in the precursor solution, the regulation of the Sn doping concentration in the ITO NCs can be achieved. Figure 1b and Figure 1c show the transmission electron microscope (TEM) images of ITO NCs synthesized with 10% (10% ITO) and 12.5% (12.5% ITO) Sn molar concentration in the precursor solutions, respectively. The obtained ITO NCs exhibit uniform size distribution with average diameters of 6 nm (Figure S1a,b). The alternation of Sn input has a negligible effect on the particle size. The elemental compositions of the ITO NCs were quantified by using energy-dispersive X-ray spectroscopy (EDX) performed on NC ensembles (Figure S2). The Sn/(Sn + In) atomic ratios were estimated as 9% and 12.5% for the ITO NCs synthesized with 10% and 12.5% Sn precursor input, respectively. The results are corresponding to the previous report and suggest that the rapid esterification is an effective method to synthesize doped NCs by simultaneously and completely decomposing the precursors.[32] Furthermore, the powder X-ray diffraction patterns of the obtained ITO NCs (Figure S3) show almost the same crystal structure as the In_2O_3 host, indicating that there is no SnO_2 phase embedded into the NCs, which is also corresponding to the previous reports.[33] The 10% ITO NCs show a prominent absorption peak at ~2300 nm, which can be attributed to the localized surface plasmon resonance (LSPR).[19] The LSPR peak is blue-shifted to ~2000 nm for 12.5% ITO NCs (Figure 1d). In addition, we found that the material also shows relatively high absorption in the UV band, which is attributed to the bandgap absorption of ITO.[34] The direct optical bandgap of the ITO NCs can be estimated from the plot of $(\alpha h\nu)^2$ versus $h\nu$ (α, absorption coefficient; $h\nu$, photon energy) by extrapolating the linear portion of the

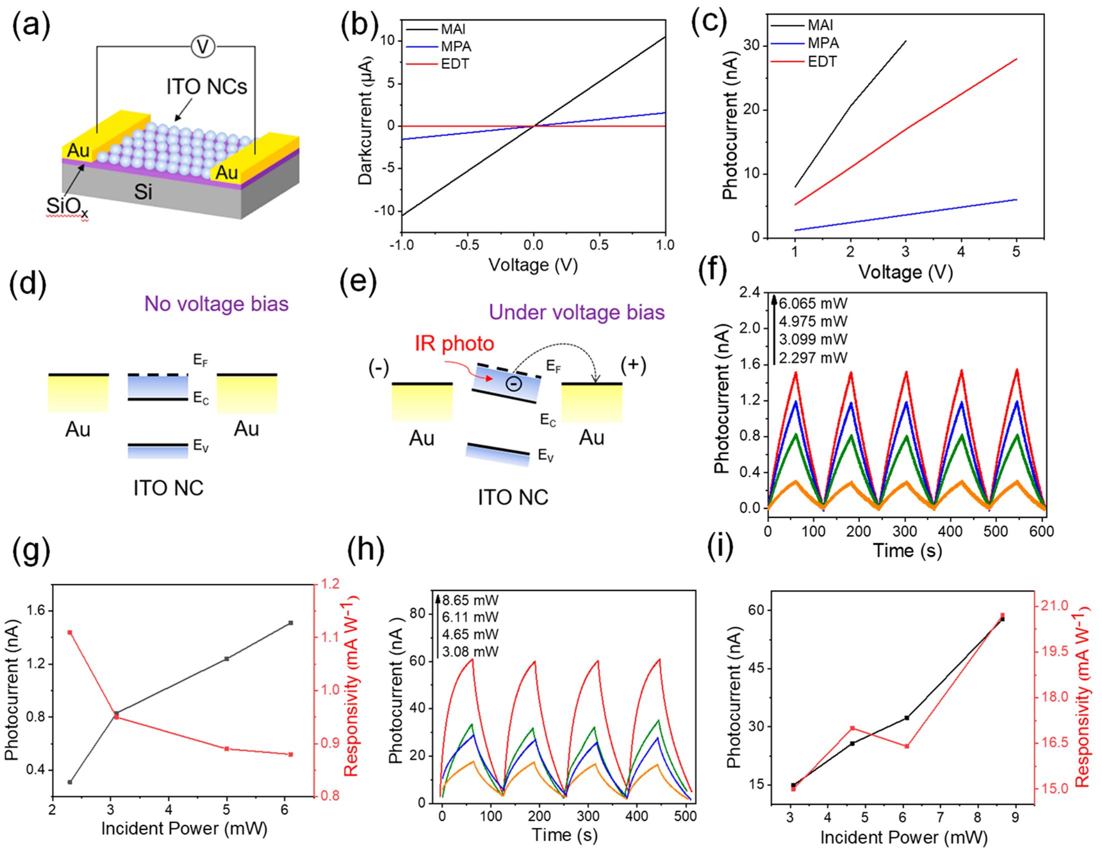

Figure 2. Photodetectors prepared on SiO_2/Si substrate characterized under 2200 and 375 nm incident light. (a) Schematic diagram of the device. (b) Dark currents of the devices fabricated by ITO NCs with different ligands. (c) Photocurrents of the devices fabricated by ITO NCs with different ligands. Energy band diagram without (d) and with (e) voltage bias. (f) *I*−*T* and (g) photocurrent and responsivity of the device under 2200 nm fabricated by ITO NCs with EDT ligand under different incident light powers. (h) *I*−*T* and (i) photocurrent and responsivity of the device under 375 nm fabricated by ITO NCs with EDT ligand under different incident light powers.

absorption curve to $\alpha = 0$ (Figure S4).[35] The bandgap of 10% ITO NCs is estimated as 3.96 eV, which increases to 3.99 eV due to the occupation of the low-lying energy levels of the conduction band at high carrier concentrations (Burstein−Moss shift).

For optoelectronic applications, it requires removing the native long-chain ligands around NCs to increase coupling and conductivity of the NC array.[36] We conducted ligand exchange experiments for ITO NCs by employing three typical small molecules (1,2-ethanedithiol (EDT), 3-mercaptopropionic acid (MPA), and methylammonium iodide (MAI)). The absorption peak of 10% ITO NCs shifts from ∼2300 to 2450 nm after the ligand exchanges, which can be attributed to the alternation of the surface environment (i.e., dielectric function of the matrix) around NCs (Figure 1e).[37] The Fourier transform IR spectroscopy (FTIR) measurements clearly confirm the native oleic acid has been substantially exchanged by the small molecules, as indicated by the decreased intensity of C−H vibration at 2750−3000 cm^{-1} (Figure 1f). Notably, the intensity of C−H vibration drops the most after EDT exchange, indicating that EDT can exchange the native oleic acid efficiently. Furthermore, ultraviolet photoelectron spectroscopy (UPS) measurements were performed to determine the energy levels of the exchanged ITO NC films. The Fermi level E_F and valence band edge E_v are extracted and displayed in Figure 1g and Table S1. The slight difference in the energy levels may be attributed to the different electric dipoles generated by the surface-bound ligand molecule.[38]

ITO NCs Photodetector Characterization. The schematic diagram of a ITO NC based photodetector device is shown in Figure 2a. During the device fabrication, the ITO NCs was first spin-coated uniformly onto Si substrate with 300 nm thermally grown SiO_2, followed by ligand exchange to replace the long-chain surface ligands as described above. Then, Au electrodes with a thickness of about 100 nm was deposited by thermal evaporation. A series of control experiments were performed to investigate the device photoresponse performance. To avoid other possible disturbances from the atmospheric environment, all subsequent photoelectric measurements were performed under vacuum with laser sources from 375 to 2200 nm. The effect of different surface ligands on the device dark current is obvious as shown in Figure 2b. The dark current of ITO NCs capped with MAI is the largest, about 11.0 μA (at 1 V), indicating the improved conductivity of the device. The dark currents of the device capped with MPA and EDT are relatively small, which are 1.8 and 1.6 μA under 1 V external bias, respectively. When the device is illuminated under 2200 nm incident light, there is a significant current boost, as shown in Figure 2c. The photocurrent gradually increases with the increase of voltage, showing a linear dependence behavior, which proves the applicability of the ITO NCs for IR photodetection. Figure 2d and Figure 2e show the energy band diagrams of the device unbiased and in the presence of biased voltage. As shown in the figure, there is no net current in the ITO NC device without biased voltage. The presence of a biased voltage leads

https://doi.org/10.1021/acsami.2c05280
ACS Appl. Mater. Interfaces 2022, 14, 24648−24658

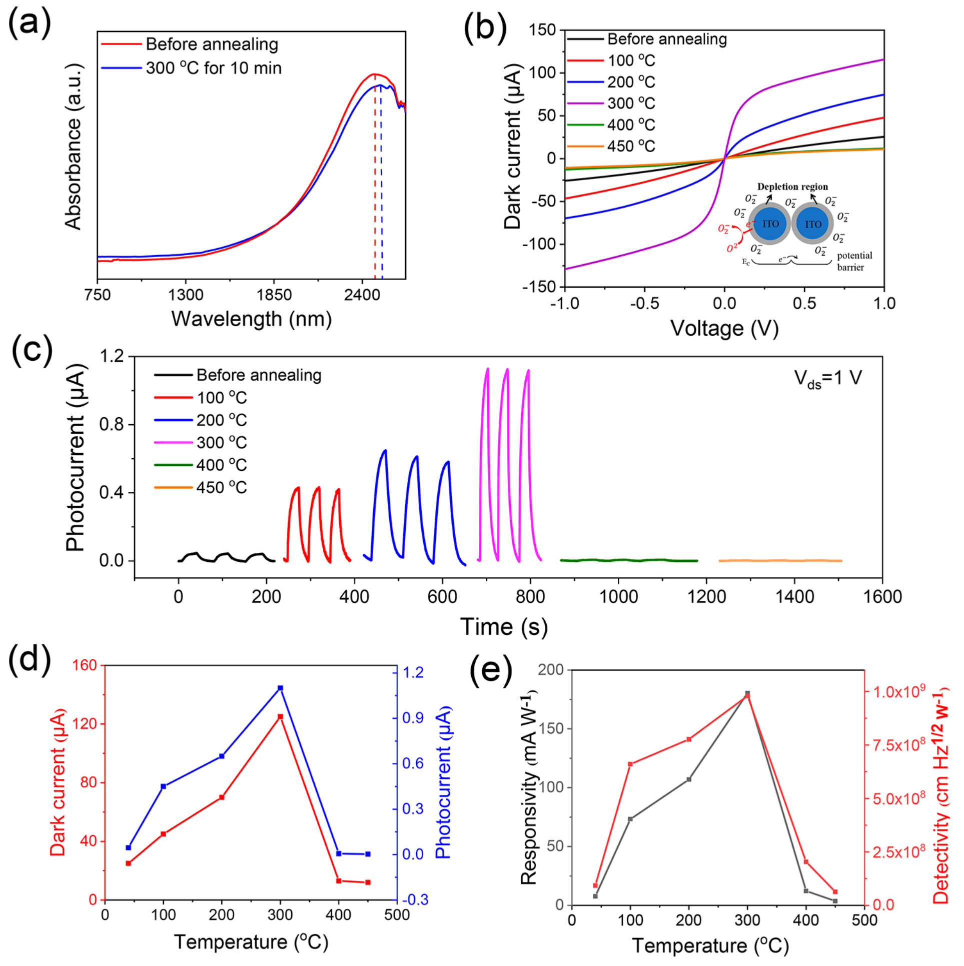

Figure 3. Device performance with different ITO NCs annealing temperatures. (a) UV−vis−NIR absorption spectra of the ITO NCs with and without annealing. (b) *I*−*V* characteristics of the devices with different annealing temperatures in dark. (c) *I*−*T* characteristics of the devices fabricated at 1 V bias voltage with different annealing temperatures. (d) Photocurrent and dark current of the device with annealing temperature. (e) Responsivity and detectivity of the device with different annealing temperatures.

to the transfer of photogenerated carriers toward metal electrodes and hence current generation. The device responsivity and detectivity can be derived using the equations $R = \frac{I_l - I_d}{P}$ and $D^* = \frac{R(A)^{1/2}}{(2qI_d)^{1/2}}$ respectively, where I_l represents the device current under illumination, I_d represents the dark current, A represents the illuminated device area, and q represents the electron charge.[39,40] The calculated results according to Figure 2b and Figure 2c are shown in Figure S5a, where ITO capped with MAI based device has the highest responsivity, while ITO capped with EDT shows the largest detectivity, which may be attributed to the improved conductivity and lower dark current of device based on ITO capped with EDT. On the basis of these preliminary results, we further investigated the properties of devices based on ITO NCs capped with EDT in the following part.

Figure 2f shows the time-dependent photocurrents (*I*−*T*) of the device under 2200 nm with different optical powers, respectively. The photocurrent of the device tends to increase with promoting optical power and also shows a good repeatability as seen from the figure. Figure S5b shows the voltage-dependent photocurrents of the device under 2200 nm, respectively. It can be seen that the photocurrent increases with the increase of bias voltage. Figure 2g depicts the power-dependent photocurrent and device responsivity. The calculated responsivity of the device decreases as the optical power increases, in good agreement with previous report.[41]

To verify the UV detection ability of the device, the photoresponse properties were investigated under 375 nm laser illumination, and the results are shown in Figure 2h,i and Figure S5c,d. When the device is irradiated by the same light source of different powers, there is a large difference in the current generated. The photocurrent of the device increases continuously with the power increasing (Figure 2h). The dark current is about 23.7 nA at an applied voltage of 1 V, while the current of the device rises to 213.3 nA at an applied optical power of 8.65 mW, with an on−off ratio of around 9 (Figure S5c). It can be seen from Figures 2h and S5d that the measured current repeated well when we varied the optical power and bias voltage. Meanwhile, it can be seen from Figure 2i that the responsivity can reach 31.3 mA W^{-1}, and the corresponding detectivity is calculated to be up to $\sim 1.3 \times 10^{10}$ cm $Hz^{1/2}$ W^{-1}, which fully illustrates the feasibility of the device for UV short-wavelength detection. It should be pointed out that the device responsivity shows a monotonic increase as we increased the incident light power, which is possibly due to the relatively weak light power we have used during the experiments in order to avoid any deterioration of ITO NCs under strong UV light emission.

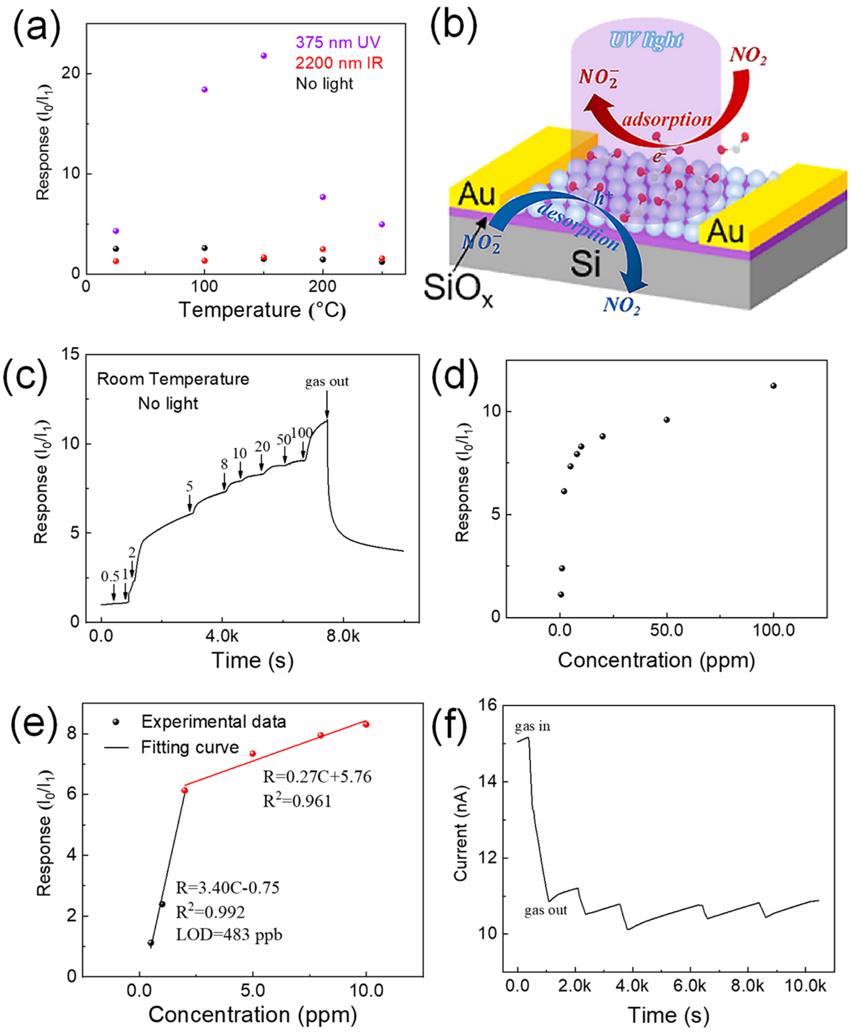

Figure 4. Gas sensing performance of ITO NCs. (a) Response of ITO NCs to 1 ppm of NO_2 at 25−250 °C. (b) Diffusion model of NO_2 molecules at the ITO NCs layer. (c) Dynamic response−recovery curves of the sensors to NO_2 in the range 0.5−100 ppm at RT without light. (d) Response of ITO NCs in the ranges from 0.5 to 100 ppm and (e) from 0.5 to 10 ppm. (f) Reproducibility of ITO NCs on successive exposure to 1 ppm of NO_2 without light at RT.

To further improve the device performance, we added an annealing step during the device preparation process. As mentioned in the previous section, we replaced the long-chain ligands on the surface of ITO NCs with short-chain ligands in order to reduce the distance between NCs. After that, the ITO NCs films were annealed in N_2 atmosphere for 10 min at different temperatures and then cooled to RT. The annealing process facilitates the NCs to bind more tightly. Figure 3a shows that the absorption peaks of the materials are significantly red-shifted after annealing, which is caused by the direct coupling enhancement of the NCs.[42] This phenomenon was also found in ITO NCs capped with different ligands, as shown in Figure S6a,b. Figure 3b shows the influence of different annealing temperatures on the electronic properties of ITO NCs. As the voltage is increased, due to the enhancement of the electric field, more electrons will be collected by the electrode per unit of time, and the current will also increase. However, when the voltage increases to a certain value, the current shows a much slower increasing trend after annealing (the purple curve in Figure 3b). This phenomenon can be explained by the following reasons. The annealed ITO NCs tend to agglomerate with each other at relatively high temperature and form an electron depletion layer at the boundaries, leading to formation of an electron potential barrier (see inset of Figure 3b).[43,44] Under small bias voltage, the enhancement of the electric field will facilitate more electrons across the barrier at the boundary, resulting in a steep increase of device current. As the bias voltage further increases, the number of electrons reaches saturation, thus causing a slower increase in the current. It is also noteworthy that the device current starts to decrease as the annealing temperature reaches 300 °C and beyond, which is possibly due to the melt of ITO NCs at high temperature. Figure 3c demonstrates the time-dependent photoresponse of the device under 2200 nm light illumination. The optical response of the device at a constant incident light power increases with annealing temperature, reaching a maximum at 300 °C. Once the temperature exceeds 300 °C, the optical response of the device decays distinctly, and photocurrent generation is basically not observed at 400 °C and beyond, which is also consistent with our previous expectation that the ITO NCs may start to melt at high temperature. Figure 3d demonstrates the device dark currents and photocurrents under different annealing temperatures, and the corresponding device responsivities and detectivities obtained at different temperatures were shown in Figure 3e. As shown in the figure, mild annealing is beneficial to the device performance, and the optimal annealing temperature is 300 °C. Under this condition, we obtained a responsivity of 177.7 mA W^{-1} and a normalized detectivity of around 1× 10^9 cm $Hz^{1/2}$ W^{-1} under 2200 nm illumination at RT. The above results prove the potential of ITO NCs for high performance UV-IR photodetection operating at RT.

Gas Sensing Properties of ITO NCs. Nitrogen dioxide (NO_2) released from industrial waste and biological fossils, at a concentration higher than 1 ppm, causes damage to the respiratory system and worsens respiratory diseases.[45] In view of this negative impact, there is an urgent need to develop the sensor that can effectively detect low-concentration NO_2 gas. We study the gas sensing characteristics of ITO NCs devices on SiO_2 substrate with the same structure as shown in Figure 4b. First, we measured the response of the sensor from RT (25 °C) to 250 °C to determine the optimum operating temperature for NO_2 sensing. Figure 4a shows the response to 1 ppm of NO_2 gas at different temperatures. It can be seen from the response trend of each curve that as the temperature increases, the response gradually increases until it reaches the optimal value and then decreases. As the temperature increases, the molecules become more active to overcome the surface energy barrier, and adsorb on the surface of ITO NCs, resulting in increase of response. But when the temperature rises further, the high temperature will cause the amount of adsorbed NO_2 to decrease, thereby reducing the response.[46] The response ratio of the sensor is defined as the ratio $R = I_0/I_1$, where I_0 and I_1 are current values of sensors in nitrogen and target gas, respectively. The response ratio of the ITO sensor to 1 ppm of NO_2 reaches 2.52 in the dark, indicating that the sensor can detect low concentrations of NO_2 at RT. The results in Figure 4a also show that the response of the sensor to NO_2 is 4.2 at RT (1 ppm of NO_2) under UV illumination, which is 1.7 times higher than that under dark conditions. However, under 2200 nm IR irradiation, the response of ITO NCs does not increase significantly. And the details of gas-sensing mechanism under light illumination will be discussed in the following part.

The gas sensing mechanism is based on the current change produced by the adsorption or desorption process on the surface of the semiconductor material in different gas environments. Figure 4b shows the diffusion model of NO_2 molecules at the ITO NCs layer. When the bias voltage is applied to the device, the electrons will move inside the ITO NCs. After the electrons move to the interface of the two NCs, it needs to cross the grain boundary barrier and enter another NC to continue transport. The current of the sensor is determined by the grain boundary barrier and the width of the depletion layer of the NCs, both of which are related to the adsorption of NO_2. The reaction, shown in the equation NO_2 (gas) + e^- → NO_2^- (ads), will occur on the surface of the ITO NCs. The choice of the light source should consider the bandgap of the semiconductor. The wide bandgap of ITO NCs means that the material can be well activated by light with higher photon energy in the UV region. Figure S7 shows the band diagram of the NO_2 sensing process in UV light. The light illumination can change the surface carrier density of the sensing material by exciting electrons from the valence band of the semiconductor,[30] and then NO_2 molecules are first adsorbed on the surface of the material to form physical adsorption NO_2 (ads). Subsequently, NO_2 (ads) will take away the electrons in the conduction band of the material and convert it into NO_2^- (ads). At the same time, the surface of the NCs loses electrons and forms an electron depletion layer. The width of the electron depletion layer will become wider as the amount of adsorbed NO_2 molecules increases so that the electron conduction channel in the NCs becomes narrower and the sensor exhibits a high resistance state. For the grain boundary barrier, its height will increase as the amount of adsorbed NO_2 gas increases, which will also cause the current of the sensor to decrease. On the one hand, the defect level caused by Sn doping can effectively inhibit the recombination of photogenerated electrons and holes and lead to an increase in the carrier concentration in the ITO NCs by the utilization of UV light, thereby significantly improving the gas detection performance at the RT. When detecting NO_2 under UV light excitation, a large amount of NO_2 participates in the gas-sensing reaction to capture electrons and adsorb on the surface of the ITO NCs, resulting in a significant decrease in the current of the ITO NCs-based gas sensor. The NO_2 gas-sensitive reaction on the surface of the sensitive material under light excitation is as follows:[47]

$$2NO_2(gas) + e^-(h\nu) \rightarrow 2NO(h\nu) + O_2^-(h\nu)$$

On the other hand, the photogenerated electron/hole pair of ITO NCs is the reason for the reduced response and recovery time. According to the equation, the excited electrons capture the NO_2 gas molecules and promote the adsorption of NO_2 to the surface of the sensor, thereby shortening the response time. Then, when the NO_2 is pumped out from the gas chamber, the photogenerated hole will also help the desorption of reaction products ($NO(h\nu)$ and $O_2^-(h\nu)$). Therefore, UV light excitation can not only improve the response of the gas sensor but also reduce the response and recovery time.

The dynamic response curve at different gas concentrations in the dark environment at RT is shown in Figure 4c. As the gas concentration increases from 0.5 to 100 ppm, the gas sensor shows a significant difference in response, which is due to a large number of absorption sites on the surface of the ITO NCs for higher concentrations of gas molecules. In Figure 4d, it can be observed that the response ratio of the gas sensor to NO_2 gradually increases as the gas concentration increases in the gas concentration range of 0.5−100 ppm. Figure 4e further illustrates the relationship between the response of the ITO NCs sensor and the gas concentration. When the NO_2 concentration is in the range of 0.5−2 ppm and 2−10 ppm, the curve can be well fitted to two linear functions with different slopes. Then, the detection limit (LOD) can be calculated using the formula LOD = 3 SD/slope, where SD is the standard deviation of the noise, and the slope is the low concentration sensitivity.[48] Therefore, the LOD is calculated and estimated to be around 483 ppb. Figure 4f represents the stability test of the sensor at RT. However, the sensor cannot fully recover during the repetitive cycle and does not exhibit satisfactory repeatability. Due to the strong interaction between gas macules and ITO NCs, the desorption of target gas from ITO NCs needs high energy, resulting in slow response and incomplete recovery, which limits their application on commercial sensing platforms. The response time or the recovery time is defined as the time to reach 90% of the total change in resistance. Figure S8 depicts the response and recovery time of the ITO NCs in NO_2 gas at different temperatures in dark. The current drops when the sensors are exposed to an oxidizing gas (NO_2), showing the typical

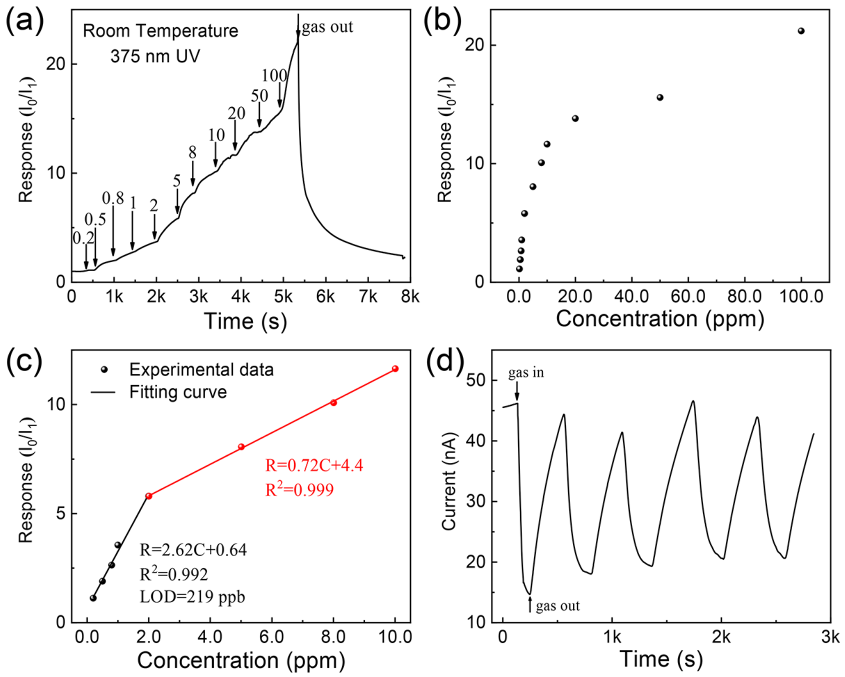

Figure 5. Gas sensing performance of ITO NCs under UV illumination. (a) Dynamic response−recovery curves of the sensors to NO_2 in the range 0.2−100 ppm at RT with 375 nm UV light. (b) Response of ITO NCs in the ranges from 0.2 to 100 ppm and (c) from 0.2 to 10 ppm with 375 nm UV light. (d) Reproducibility of ITO NCs on successive exposure to 1 ppm of NO_2 with 375 nm UV light at RT.

Table 1. Comparison of the Gas Sensing Properties of Doped In_2O_3 for NO_2

material	structure	T_m (°C)	LOD (ppm)	response	T_{res}/T_{recov} (s)	ref
Fe-doped In_2O_3	nanorods	80	0.1	82 (2 ppm)	75/60	52
Sn−In_2O_3	nanofibers	90	1	44.6 (1 ppm)	106/85	53
Pd−In_2O_3	3DOM[a]	RT	0.1	980 (0.5 ppm)	270/286	54
In_2O_3	nanosheets	100	0.05	5.3 (1 ppm)	289/478	55
In_2O_3	microcubes	60	0.5	∼6.5 (1 ppm)	−/−	56
Rb−In_2O_3	microspheres	75	0.004	10.2 (100 ppb)	210/65	57
SnO_2−boron nitride	nanotubes	100	0.25	∼2610 (5 ppm)	38/40	58
MoS_2−SnO_2	nanoflakes	RT	0.01	34.47 (100 ppm)	2.2/10.54	59
SnO_2	nanotoast	50	0.1	105.2 (10 ppm)	10/37.2	60
ITO	nanocrystals	RT	0.22	4.2 (1 ppm)	210/554.2	this work

[a] 3DOM: three dimensionally ordered macroporous.

behavior of n-type semiconductors. At RT and 100 °C, the response times of the sensor is 563.4 and 104 s, respectively, and it cannot be fully recovered. With increasing working temperature, the response/recovery times are found to be 125 s/551 s, 165 s/481 s, and 308.96 s/369.54 s at operating temperatures of 150 °C, 200 °C, and 250 °C, respectively. Notably, as the operating temperature increases, the current of the sensor can be restored to the initial state. However, high operating temperature may reduce the working life of the sensor and increase the complexity of manufacturing and make the sensor sensitivity degenerated due to the thermally induced ripening of nanoparticles.[49,50]

Therefore, we use an external light source to achieve fast response and complete recovery. Figure S9 describes the response/recovery time of ITO NCs under 12.5 mW cm^{-2} of 375 nm UV irradiation at the different operating temperatures. Figure S8a shows the change of the transient current of the sensor at RT. Compared with the baseline current (15 nA) in the dark state, the baseline current of the sensor increases (45 nA) in Figure S9a due to the generation of photogenerated electrons during UV irradiation. Moreover, the response time and recovery time of ITO NCs are 156.8 and 554.2 s at RT, respectively, which are shorter than those in the dark. In addition, in Figure S10a, we can find that under 2200 nm IR light irradiation, the response time of the ITO NC sensor is 184 s, and the recovery rate is only 17% within 900 s at RT, showing slight enhancement compared to that in the dark, but inferior to that under UV light illumination.

In practical applications, real-time detection plays an important role in the detection of toxic gases. Figure 5a shows the dynamic response of the ITO sensor with increasing NO_2 concentration under UV light illumination. The response ratio and response times are 1.17 and 21.5 s for 0.2 ppm, 1.9 and 250.5 s for 0.5 ppm, and 4.2 and 280.2 s for 1 ppm, respectively. As shown in Figure 5b,c, the relationship between the response and the gas concentration can still be fitted to two linear functions with different slopes. Compared with that in the dark (483 ppb), a lower LOD (219 ppb) is obtained under UV irradiation. The LOD of the sensor is lower than the allowable exposure limit of nitrogen dioxide (5 ppm) specified in "Air Pollutant Limits" of the Occupational Safety and Health Administration (OSHA).[51] Regarding the repeatability of the sensor, we measured several response/recovery periods of the sensor to 1 ppm of NO_2, as shown in Figure 5d, which shows that in each cycle of NO_2 adsorption and desorption, the sensor remains stable and can be restored to the initial current value. In comparison, as shown in Figure S11 under 2200 nm IR illumination, the sensor cannot recover to the initial current, and the sensitivity is less enhanced compared to that under UV illumination.

To demonstrate the potential effect of other interfering gases on the ITO NCs at RT, the devices were exposed to several other gases, including formaldehyde, ammonia, and sulfur dioxide (Figure S12). Among the gases tested, the devices exhibited high selectivity for 1 ppm of NO_2 under UV light irradiation, while the devices did not possess good selectivity in the dark or IR light. The above results indicated that the introduction of UV excitation is an effective approach to enhance the sensitivity to NO_2 at RT. A comparison with other NO_2 sensors based on In_2O_3 nanomaterials is listed in Table 1.[52−60] Until now, various In_2O_3 and SnO_2 nanostructures have been utilized to detect NO_2, including Fe-doped In_2O_3 nanorods, Sn−In_2O_3 nanofibers, Pt−In_2O_3 3DOM, In_2O_3 nanosheets, In_2O_3 microcubes, Rb−In_2O_3 microspheres, SnO_2−boron nitride nanotube, SnO_2 nanotoast, etc. Our sensor shows a relatively low operating temperature but comparatively quick response time and comparable LOD compared to other In_2O_3 sensors. Accordingly, ITO NC is a promising sensing material for detecting NO_2 at RT because of its high response, lower LOD, and rapid response speeds.

CONCLUSION

In summary, we have demonstrated the feasibility of utilizing ITO NCs for a multifunctional sensing system. The system can simultaneously detect a variety of environmental parameters, including the changes in UV and IR light intensity and NO_2 gas concentration. We have combined them with SiO_2 substrates to realize a photodetector with a responsivity of 31.3 mA W^{-1} and a normalized detectivity of around 10^{10} cm $Hz^{1/2}$ W^{-1} under UV illumination of 375 nm and a responsivity of 177.7 mA W^{-1} and a normalized detectivity of $\sim 10^9$ cm $Hz^{1/2}$ W^{-1} under IR illumination of 2200 nm. In addition, by varying the doping amount of Sn in the ITO NCs, the absorption peaks are modulated, which also provides the theoretical feasibility for future realization of a wavelength-tunable IR photodetector. The results on the gas sensing performance of ITO NCs exhibited a high response (2.52) to 1 ppm of NO_2 at RT. The performance of the device is further promoted under UV light with a higher response of 4.2−1 ppm of NO_2 which is 1.7 times that in the dark. Our research provides a new platform for the development of multifunctional device applications using zero-dimension nanomaterials, potentially for integrated smart microsystems.

ASSOCIATED CONTENT

Supporting Information

The Supporting Information is available free of charge at https://pubs.acs.org/doi/10.1021/acsami.2c05280.

> Full details for particle size distribution, photodetector performance, characterization results, and gas sensing performance (PDF)

AUTHOR INFORMATION

Corresponding Authors

Zeke Liu − *Institute of Functional Nano & Soft Materials (FUNSOM), Jiangsu Key Laboratory for Carbon-Based Functional Materials & Devices, Joint International Research Laboratory of Carbon-Based Functional Materials and Devices, Soochow University, Suzhou 215123, P. R. China;* orcid.org/0000-0002-2507-4386; Email: zkliu@suda.edu.cn

Baoquan Sun − *Institute of Functional Nano & Soft Materials (FUNSOM), Jiangsu Key Laboratory for Carbon-Based Functional Materials & Devices, Joint International Research Laboratory of Carbon-Based Functional Materials and Devices, Soochow University, Suzhou 215123, P. R. China;* orcid.org/0000-0002-4507-4578; Email: bqsun@suda.edu.cn

Shaojuan Li − *State Key Laboratory of Applied Optics, Changchun Institute of Optics, Fine Mechanics and Physics, Chinese Academy of Sciences, Changchun 130033, P. R. China; University of Chinese Academy of Sciences (UCAS), Beijing 100049, P. R. China;* orcid.org/0000-0002-0504-2934; Email: lishaojuan@ciomp.ac.cn

Authors

Chang Shu − *Institute of Functional Nano & Soft Materials (FUNSOM), Jiangsu Key Laboratory for Carbon-Based Functional Materials & Devices, Joint International Research Laboratory of Carbon-Based Functional Materials and Devices, Soochow University, Suzhou 215123, P. R. China*

Nan Zhang − *State Key Laboratory of Applied Optics, Changchun Institute of Optics, Fine Mechanics and Physics, Chinese Academy of Sciences, Changchun 130033, P. R. China; University of Chinese Academy of Sciences (UCAS), Beijing 100049, P. R. China*

Yiyuan Gao − *Institute of Functional Nano & Soft Materials (FUNSOM), Jiangsu Key Laboratory for Carbon-Based Functional Materials & Devices, Joint International Research Laboratory of Carbon-Based Functional Materials and Devices, Soochow University, Suzhou 215123, P. R. China*

Junru An − *State Key Laboratory of Applied Optics, Changchun Institute of Optics, Fine Mechanics and Physics, Chinese Academy of Sciences, Changchun 130033, P. R. China; University of Chinese Academy of Sciences (UCAS), Beijing 100049, P. R. China*

Xin Wen − *Institute of Functional Nano & Soft Materials (FUNSOM), Jiangsu Key Laboratory for Carbon-Based Functional Materials & Devices, Joint International Research Laboratory of Carbon-Based Functional Materials and Devices, Soochow University, Suzhou 215123, P. R. China*

Wanli Ma − *Institute of Functional Nano & Soft Materials (FUNSOM), Jiangsu Key Laboratory for Carbon-Based Functional Materials & Devices, Joint International Research Laboratory of Carbon-Based Functional Materials and Devices, Soochow University, Suzhou 215123, P. R. China*

Complete contact information is available at: https://pubs.acs.org/10.1021/acsami.2c05280

Author Contributions

‖C.S., N.Z., and Y.G. contributed equally to this work. C.S. conceived and designed the experiments. C.S., N.Z., and Y.G. carried out the synthesis of ITO NCs and the experiments of the photodetector and the gas sensor. C.S. and Y.G. performed TEM and spectra studies. C.S. and N.Z. wrote the manuscript.

All authors contributed to the discussion and revision of the paper. All authors have given approval to the final version of the manuscript

Notes

The authors declare no competing financial interest.

■ ACKNOWLEDGMENTS

The authors acknowledge support from the National Natural Science Foundation of China (Grants 62022081 and 61974099), the Science Fund for Creative Research Groups of the National Natural Science Foundation of China (Grant 62121005), the Natural Science Foundation of Jilin Province (Grants 20210101173JC and 21ZY03), and China Postdoctoral Science Foundation (Grants 2021TQ0358 and 2021M703128). The project was also supported by the State Key Laboratory of Applied Optics (Grant SKLAO2020001A03). Z.L. and B.S. also acknowledge the support from Suzhou Key Laboratory of Functional Nano & Soft Materials, Collaborative Innovation Center of Suzhou Nano Science & Technology, and the 111 Project.

■ REFERENCES

(1) Xu, K.; Lu, Y.; Takei, K. Multifunctional Skin-Inspired Flexible Sensor Systems for Wearable Electronics. *Adv. Mater. Technol.* **2019**, *4* (3), 1800628.

(2) Song, Y.; Gao, W.; Zhang, H. *Integrated Smart Micro-Systems Towards Personalized Healthcare*; John Wiley & Sons, 2021; p 15.

(3) Kim, J.; Lee, M.; Shim, H. J.; Ghaffari, R.; Cho, H. R.; Son, D.; Jung, Y. H.; Soh, M.; Choi, C.; Jung, S.; et al. Stretchable Silicon Nanoribbon Electronics for Skin Prosthesis. *Nat. Commun.* **2014**, *5* (1), 5747.

(4) Yao, Q.; Ren, G.; Xu, K.; Zhu, L.; Khan, H.; Mohiuddin, M.; Khan, M. W.; Zhang, B. Y.; Jannat, A.; Haque, F.; et al. 2D Plasmonic Tungsten Oxide Enabled Ultrasensitive Fiber Optics Gas Sensor. *Adv. Opt. Mater.* **2019**, *7* (24), 1901383.

(5) An, X.; Liu, F.; Jung, Y. J.; Kar, S. Tunable Graphene−Silicon Heterojunctions for Ultrasensitive Photodetection. *Nano Lett.* **2013**, *13* (3), 909−916.

(6) Fernández-Domínguez, A. I.; García-Vidal, F. J.; Martín-Moreno, L. Unrelenting Plasmons. *Nat. Photonics* **2017**, *11* (1), 8−10.

(7) Tame, M. S.; McEnery, K. R.; Özdemir, S. K.; Lee, J.; Maier, S. A.; Kim, M. S. Quantum Plasmonics. *Nat. Phys.* **2013**, *9* (6), 329−340.

(8) Paliwal, A.; Sharma, A.; Tomar, M.; Gupta, V. Room Temperature Detection of NO_2 Gas Using Optical Sensor Based on Surface Plasmon Resonance Technique. *Sens. Actuators B* **2015**, *216*, 497.

(9) Patil, P. O.; Pandey, G. R.; Patil, A. G.; Borse, V. B.; Deshmukh, P. K.; Patil, D. R.; Tade, R. S.; Nangare, S. N.; Khan, Z. G.; Patil, A. M.; et al. Graphene-based Nanocomposites for Sensitivity Enhancement of Surface Plasmon Resonance Sensor for Biological and Chemical Sensing: A Review. *Biosens. Bioelectron.* **2019**, *139*, 111324.

(10) Wang, G.; Li, L.; Fan, W.; Wang, R.; Zhou, S.; Lü, J. T.; Gan, L.; Zhai, T. Interlayer Coupling Induced Infrared Response in WS_2/MoS_2 Heterostructures Enhanced by Surface Plasmon Resonance. *Adv. Funct. Mater.* **2018**, *28* (22), 1800339.

(11) Sobhani, A.; Knight, M. W.; Wang, Y.; Zheng, B.; King, N. S.; Brown, L. V.; Fang, Z.; Nordlander, P.; Halas, N. J. Narrowband Photodetection in the Near-Infrared with a Plasmon-Induced Hot Electron Device. *Nat. Commun.* **2013**, *4*, 1038.

(12) Sun, T.; Wang, Y.; Yu, W.; Wang, Y.; Dai, Z.; Liu, Z.; Shivananju, B. N.; Zhang, Y.; Fu, K.; Shabbir, B.; Ma, W.; Li, S.; Bao, Q. Flexible Broadband Graphene Photodetectors Enhanced by Plasmonic $Cu_{3-x}P$ Colloidal Nanocrystals. *Small* **2017**, *13* (42), 1701881.

(13) Liu, Z. K.; Mu, H. R.; Xiao, S.; Wang, R. B.; Wang, Z. T.; Wang, W. W.; Wang, Y. J.; Zhu, X. X.; Lu, K. Y.; Zhang, H.; Lee, S. T.; Bao, Q. L.; Ma, W. L. Pulsed Lasers Employing Solution-Processed Plasmonic $Cu_{3-x}P$ Colloidal Nanocrystals. *Adv. Mater.* **2016**, *28* (18), 3535.

(14) Liu, Z.; Zhong, Y.; Shafei, I.; Jeong, S.; Wang, L.; Nguyen, H. T.; Sun, C. J.; Li, T.; Chen, J.; Chen, L.; Losovyj, Y.; Gao, X.; Ma, W.; Ye, X. Broadband Tunable Mid-Infrared Plasmon Resonances in Cadmium Oxide Nanocrystals Induced by Size-Dependent Non-stoichiometry. *Nano Lett.* **2020**, *20* (4), 2821−2828.

(15) Agrawal, A.; Cho, S. H.; Zandi, O.; Ghosh, S.; Johns, R. W.; Milliron, D. J. Localized Surface Plasmon Resonance in Semiconductor Nanocrystals. *Chem. Rev.* **2018**, *118* (6), 3121−3207.

(16) Liu, Z.; Zhong, Y.; Shafei, I.; Borman, R.; Jeong, S.; Chen, J.; Losovyj, Y.; Gao, X.; Li, N.; Du, Y.; Sarnello, E.; Li, T.; Su, D.; Ma, W.; Ye, X. Tuning Infrared Plasmon Resonances in Doped Metal-Oxide Nanocrystals through Cation-Exchange reactions. *Nat. Commun.* **2019**, *10* (1), 1394.

(17) Gong, Y.; Lu, J.; Cheng, S.-L.; Nishi, Y.; Vuckovic, J. Plasmonic Enhancement of Emission from Si-Nanocrystals. *Appl. Phys. Lett.* **2009**, *94* (1), 013106.

(18) Xia, Z.; Li, P.; Wang, Y.; Song, T.; Zhang, Q.; Sun, B. Solution-Processed Gold Nanorods Integrated with Graphene for Near-Infrared Photodetection via Hot Carrier Injection. *ACS Appl. Mater. Interfaces* **2015**, *7* (43), 24136−24141.

(19) Qu, J.; Livache, C.; Martinez, B.; Greboval, C.; Chu, A.; Meriggio, E.; Ramade, J.; Cruguel, H.; Xu, X. Z.; Proust, A.; Volatron, F.; Cabailh, G.; Goubet, N.; Lhuillier, E. Transport in ITO Nanocrystals with Short- to Long-Wave Infrared Absorption for Heavy-Metal-Free Infrared Photodetection. *ACS Appl. Nano Mater.* **2019**, *2* (3), 1621−1630.

(20) Staller, C. M.; Gibbs, S. L.; Saez Cabezas, C. A.; Milliron, D. J. Quantitative Analysis of Extinction Coefficients of Tin-Doped Indium Oxide Nanocrystal Ensembles. *Nano Lett.* **2019**, *19* (11), 8149−8154.

(21) Kumar, A.; Zhou, C. The Race to Replace Tin-Doped Indium Oxide: Which Material Will Win? *ACS Nano* **2010**, *4* (1), 11−14.

(22) Ho, P. K. H.; Kim, J. S.; Burroughes, J. H.; Becker, H.; Li, S. F. Y.; Brown, T. M.; Cacialli, F.; Friend, R. H. Molecular-Scale Interface Engineering for Polymer Light-Emitting Diodes. *Nature* **2000**, *404* (6777), 481−84.

(23) Tan, Z. K.; Moghaddam, R. S.; Lai, M. L.; Docampo, P.; Higler, R.; Deschler, F.; Price, M.; Sadhanala, A.; Pazos, L. M.; Credgington, D.; Hanusch, F.; Bein, T.; Snaith, H. J.; Friend, R. H. Bright Light-Emitting Diodes Based on Organometal Halide Perovskite. *Nat. Nanotechnol.* **2014**, *9* (9), 687−692.

(24) Li, Y. Molecular Design of Photovoltaic Materials for Polymer Solar Cells: toward Suitable Electronic Energy Levels and Broad Absorption. *Acc. Chem. Res.* **2012**, *45* (5), 723−733.

(25) Hecht, D. S.; Hu, L.; Irvin, G. Emerging Transparent Electrodes Based on Thin Films of Carbon Nanotubes, Graphene, And Metallic Nanostructures. *Adv. Mater.* **2011**, *23* (13), 1482−1513.

(26) Ma, Z.-H.; Yu, R.-T.; Song, J.-M. Facile Synthesis of Pr-doped In_2O_3 Nanoparticles and Their High Gas Sensing Performance for Ethanol. *Sens. Actuators B* **2020**, *305*, 127377.

(27) Gu, F.; Li, C.; Han, D.; Wang, Z. Manipulating the Defect Structure (V_O) of In_2O_3 Nanoparticles for Enhancement of Formaldehyde Detection. *ACS Appl. Mater. Interfaces* **2018**, *10* (1), 933−942.

(28) Zhao, S.; Shen, Y.; Zhou, P.; Hao, F.; Xu, X.; Gao, S.; Wei, D.; Ao, Y.; Shen, Y. Enhanced NO_2 Sensing Performance of ZnO Nanowires Functionalized with Ultra-fine In_2O_3 Nanoparticles. *Sens. Actuators B* **2020**, *308*, 127729.

(29) Liu, X.; Jiang, L.; Jiang, X.; Tian, X.; Sun, X.; Wang, Y.; He, W.; Hou, P.; Deng, X.; Xu, X. Synthesis of Ce-doped In_2O_3 Nanostructure for Gas Sensor Applications. *Appl. Surf. Sci.* **2018**, *428*, 478.

(30) Kumar, R.; Liu, X.; Zhang, J.; Kumar, M. Room-temperature Gas Sensors under Photoactivation: from Metal Oxides to 2D Materials. *Nano-micro Lett.* **2020**, *12* (1), 164.

(31) Wu, E.; Xie, Y.; Yuan, B.; Zhang, H.; Hu, X.; Liu, J.; Zhang, D. Ultrasensitive and Fully Reversible NO_2 Gas Sensing Based on P-Type $MoTe_2$ under Ultraviolet Illumination. *ACS Sens* **2018**, *3* (9), 1719−1726.

(32) Ito, D.; Yokoyama, S.; Zaikova, T.; Masuko, K.; Hutchison, J. E. Synthesis of Ligand-Stabilized Metal Oxide Nanocrystals and Epitaxial Core/Shell Nanocrystals via a Lower-Temperature Esterification Process. *ACS Nano* **2014**, *8* (1), 64−75.

(33) Jansons, A. W.; Koskela, K. M.; Crockett, B. M.; Hutchison, J. E. Transition Metal-Doped Metal Oxide Nanocrystals: Efficient Substitutional Doping through A Continuous Growth Process. *Chem. Mater.* **2017**, *29* (19), 8167−8176.

(34) Sakamoto, M.; Kawawaki, T.; Kimura, M.; Yoshinaga, T.; Vequizo, J. J. M.; Matsunaga, H.; Ranasinghe, C. S. K.; Yamakata, A.; Matsuzaki, H.; Furube, A.; Teranishi, T. Clear and Transparent Nanocrystals for Infrared-Responsive Carrier Transfer. *Nat. Commun.* **2019**, *10*, 406.

(35) Gordon, T. R.; Paik, T.; Klein, D. R.; Naik, G. V.; Caglayan, H.; Boltasseva, A.; Murray, C. B. Shape-Dependent Plasmonic Response and Directed Self-Assembly in A New Semiconductor Building Block, Indium-Doped Cadmium Oxide (ICO). *Nano Lett.* **2013**, *13* (6), 2857−2863.

(36) Kumar, R.; Goel, N.; Kumar, M. UV-Activated MoS_2 Based Fast and Reversible NO_2 Sensor at Room Temperature. *ACS Sens* **2017**, *2* (11), 1744−1752.

(37) Mashkov, O.; Körfer, J.; Eigen, A.; Yousefi-Amin, A.-A.; Killilea, N.; Barabash, A.; Sytnyk, M.; Khansur, N.; Halik, M.; Webber, K. G.; Heiss, W. Effect of Ligand Treatment on the Tuning of Infrared Plasmonic Indium Tin Oxide Nanocrystal Electrochromic Devices. *Adv. Eng. Mater.* **2020**, *22* (9), 2000112.

(38) Brown, P. R.; Kim, D.; Lunt, R. R.; Zhao, N.; Bawendi, M. G.; Grossman, J. C.; Bulovic, V. Energy Level Modification in Lead Sulfide Quantum Dot Thin Films through Ligand Exchange. *ACS Nano* **2014**, *8* (6), 5863−5872.

(39) Wang, F.; Luo, P.; Zhang, Y.; Huang, Y.; Zhang, Q.; Li, Y.; Zhai, T. Band Structure Engineered Tunneling Heterostructures for High-Performance Vsible and Near-Infrared Photodetection. *Sci. China Mater.* **2020**, *63* (8), 1537−1547.

(40) Wang, Y.; Gan, L.; Chen, J.; Yang, R.; Zhai, T. Achieving Highly Uniform Two-Dimensional PbI_2 Flakes for Photodetectors via Space Confined Physical Vapor Deposition. *Sci. Bull.* **2017**, *62* (24), 1654−1662.

(41) Koppens, F. H. L.; Mueller, T.; Avouris, P.; Ferrari, A. C.; Vitiello, M. S.; Polini, M. Photodetectors Based on Graphene, Other Two-Dimensional Materials and Hybrid Systems. *Nat. Nanotechnol.* **2014**, *9* (10), 780−793.

(42) Diroll, B. T.; Gordon, T. R.; Gaulding, E. A.; Klein, D. R.; Paik, T.; Yun, H. J.; Goodwin, E. D.; Damodhar, D.; Kagan, C. R.; Murray, C. B. Synthesis of N-Type Plasmonic Oxide Nanocrystals and the Optical and Electrical Characterization of Their Transparent Conducting Films. *Chem. Mater.* **2014**, *26* (15), 4579−4588.

(43) Sun, Y.-F.; Liu, S.-B.; Meng, F.-L.; Liu, J.-Y.; Jin, Z.; Kong, L.-T.; Liu, J.-H. Metal Oxide Nanostructures and Their Gas Sensing Properties: A Review. *Sensors* **2012**, *12* (3), 2610−2631.

(44) Zandi, O.; Agrawal, A.; Shearer, A. B.; Reimnitz, L. C.; Dahlman, C. J.; Staller, C. M.; Milliron, D. J. Impacts of Surface Depletion on The Plasmonic Properties of Doped Semiconductor Nanocrystals. *Nat. Mater.* **2018**, *17* (8), 710.

(45) Hu, J.; Zou, C.; Su, Y.; Li, M.; Han, Y.; Kong, E. S.-W.; Yang, Z.; Zhang, Y. An ultrasensitive NO_2 Gas Sensor Based on A Hierarchical Cu_2O/CuO Mesocrystal Nanoflower. *J. Mater. Chem. A* **2018**, *6* (35), 17120−17131.

(46) Zhang, N.; Lu, Y.; Fan, Y.; Zhou, J.; Li, X.; Adimi, S.; Liu, C.; Ruan, S. Metal−Organic Framework-Derived ZnO/$ZnCo_2O_4$ Microspheres Modified by Catalytic PdO Nanoparticles for Sub-ppm-Level Formaldehyde Detection. *Sens. Actuators B* **2020**, *315*, 128118.

(47) Hsueh, T.-J.; Peng, C.-H.; Chen, W.-S. A Transparent Zno Nanowire MEMS Gas Sensor Prepared by An ITO Micro-Heater. *Sens. Actuators B* **2020**, *304*, 127319.

(48) Fan, J.-L.; Hu, X.-F.; Fu, C.; Qin, W.-W.; Min, X.-J.; Zhao, J.-W.; Luo, L.-B.; Zhang, W. Few-layer $PdSe_2$ Nanofilm/Si Heterojunction for Sensing NO_2 at Room Temperature. *ACS Appl. Nano Mater.* **2021**, *4* (7), 7358−7370.

(49) Le, H.-J.; Van Dao, D.; Yu, Y.-T. Superfast and Efficient Hydrogen Gas Sensor Using PdAu Alloy@ZnO Core−Shell Nanoparticles. *J. Mater. Chem. A* **2020**, *8* (26), 12968−12974.

(50) Zito, C. A.; Perfecto, T. M.; Dippel, A. C.; Volanti, D. P.; Koziej, D. Low-Temperature Carbon Dioxide Gas Sensor Based on Yolk-Shell Ceria Nanospheres. *ACS Appl. Mater. Interfaces* **2020**, *12* (15), 17745−17751.

(51) Spence, A. The Development of A Model Program for The Effective Management of Biomedical Waste in The Caribbean. A Review of Barriers within Public Hospitals in The Caribbean. Master of Science Thesis, Rochester Institute of Technology, 2010.

(52) Du, W.; Si, W.; Zhao, J.; Wang, F.; Han, Z.; Wang, Z.; Liu, W.; Lu, G.; Liu, J.; Wu, L. Mesoporous Fe-doped In_2O_3 Nanorods Derived from Metal-Organic Frameworks for Enhanced Nitrogen Dioxide Detection at Low Temperature. *Ceram. Int.* **2020**, *46* (12), 20385−20394.

(53) Ri, J.; Li, X.; Shao, C.; Liu, Y.; Han, C.; Li, X.; Liu, Y. Sn-Doping Induced Oxygen Vacancies on The Surface of The In_2O_3 Nanofibers and Their Promoting Effect on Sensitive NO_2 Detection at Low Temperature. *Sens. Actuators B* **2020**, *317*, 128194.

(54) Wang, Z.; Men, G.; Zhang, R.; Gu, F.; Han, D. Pd Loading Induced Excellent NO_2 Gas Sensing of 3DOM In_2O_3 at Room Temperature. *Sens. Actuators B* **2018**, *263*, 218.

(55) Yang, W.; Chen, H.; Lu, J. Assembly of Stacked In_2O_3 Nanosheets for Detecting Trace NO_2 with Ultrahigh Selectivity and Promoted Recovery. *Appl. Surf. Sci.* **2021**, *539*, 148217.

(56) Navale, S. T.; Liu, C.; Yang, Z.; Patil, V. B.; Cao, P.; Du, B.; Mane, R. S.; Stadler, F. J. Low-Temperature Wet Chemical Synthesis Strategy of In_2O_3 for Selective Detection of NO_2 down to ppb Levels. *J. Alloys Compd.* **2018**, *735*, 2102.

(57) Wang, Y.; Yao, L.; Xu, L.; Wu, W.; Lin, W.; Zheng, C.; Feng, Y.; Gao, X. Enhanced NO_2 Gas Sensing Properties Based on Rb-Doped Hierarchical Flower-like In_2O_3 Microspheres at Low-Temperature. *Sens. Actuators B* **2021**, *332*, 129497.

(58) Sharma, B.; Sharma, A.; Myung, J.-h. Selective ppb-Level NO_2 Gas Sensor Based on SnO_2-Boron Nitride Nanotubes. *Sens. Actuators B* **2021**, *331*, 129464.

(59) Bai, X.; Lv, H.; Liu, Z.; Chen, J.; Wang, J.; Sun, B.; Zhang, Y.; Wang, R.; Shi, K. Thin-layered MoS_2 Nanoflakes Vertically Grown on SnO_2 Nanotubes as Highly Effective Room-Temperature NO_2 Gas Sensor. *J. Hazard. Mater.* **2021**, *416*, 125830.

(60) Li, J.; Yang, M.; Cheng, X.; Zhang, X.; Guo, C.; Xu, Y.; Gao, S.; Major, Z.; Zhao, H.; Huo, L. Fast Detection of NO_2 by Porous SnO_2 Nanotoast Sensor at Low Temperature. *J. Hazard. Mater.* **2021**, *419*, 126414.